

# Melt-rich channel observed at the lithosphere–asthenosphere boundary

S. Naif<sup>1</sup>, K. Key<sup>1</sup>, S. Constable<sup>1</sup> & R. L. Evans<sup>2</sup>

The lithosphere–asthenosphere boundary (LAB) separates rigid oceanic plates from the underlying warm ductile asthenosphere. Although a viscosity decrease beneath this boundary is essential for plate tectonics, a consensus on its origin remains elusive. Seismic studies identify a prominent velocity discontinuity at depths thought to coincide with the LAB but disagree on its cause<sup>1–5</sup>, generally invoking either partial melting<sup>6</sup> or a mantle dehydration boundary<sup>7</sup> as explanations. Here we use sea-floor magnetotelluric data to image the electrical conductivity of the LAB beneath the edge of the Cocos plate at the Middle America trench offshore of Nicaragua. Underneath the resistive oceanic lithosphere, the magnetotelluric data reveal a high-conductivity layer confined to depths of 45 to 70 kilometres. Because partial melts are stable at these depths in a warm damp mantle<sup>8</sup>, we interpret the conductor to be a partially molten layer capped by an impermeable frozen lid that is the base of the lithosphere. A conductivity anisotropy parallel to plate motion indicates that this melt has been sheared into flow-aligned tube-like structures<sup>9</sup>. We infer that the LAB beneath young plates consists of a thin, partially molten, channel of low viscosity that acts to decouple the overlying brittle lithosphere from the deeper convecting mantle. Because this boundary layer has the potential to behave as a lubricant to plate motion, its proximity to the trench may have implications for subduction dynamics.

The passive magnetotelluric method uses naturally occurring magnetic fields and induced electric fields to probe mantle electrical conductivity structure. Because pure melts are at least two orders of magnitude more conductive than a typical peridotite, mantle conductivity can be greatly increased by small amounts of partial melt<sup>10</sup>, whereas conductivity depends to a much lesser extent on mantle temperature and hydration state<sup>11</sup>. This large conductivity contrast makes magnetotelluric soundings highly sensitive to the presence of mantle partial melts.

We deployed 50 broadband electromagnetic stations across a single 280-km-long profile that extended from the Cocos plate abyssal plain, across the trench, and onto the continental shelf, amounting to the largest subduction zone electromagnetic deployment to date (Fig. 1). Data from high-frequency controlled-source electromagnetic profiling revealed that the pervasive extensional bending faults on the trench outer rise are porous channels that allow for deep crustal hydration and serpentinization of the uppermost mantle<sup>12</sup>. The lower-frequency magnetotelluric data considered here target deeper conductivity structure in the lithosphere and asthenosphere. We extended the instrument array far onto the abyssal plain to image what we expected to be unremarkable conductivity beneath the oceanic plate, which would provide a baseline for comparisons with conductivity features found beneath the trench axis and continental margin.

We converted the observed magnetotelluric responses into a two-dimensional conductivity model using a nonlinear regularized inversion that solved for the triaxially anisotropic conductivity tensor of 10,000 mesh cells<sup>13,14</sup>. Figure 2a shows the horizontal resistivity (reciprocal of

conductivity) component aligned in the direction of plate motion. All three tensor components are shown in Supplementary Fig. 3.

Landward of the trench, the magnetotelluric data reveal a resistive subducting slab and mantle, with a notable correlation between the location of earthquakes and high resistivity (Fig. 2a). The widespread distribution of earthquakes and high resistivity indicates that the brittle slab is rupturing over a wide depth range (rather than the rupturing being concentrated along the plate interface), consistent with high resistivity indicating a relatively cold, fluid-free mantle.

The conductivity becomes laterally uniform westward of the trench. A veneer of low-resistivity sediments and extrusive volcanics overlie a highly resistive lithosphere, typical of oceanic plate structure<sup>15</sup>. Below this, we find an anomalously conductive, horizontally extensive layer of 4–6  $\Omega$  m at 45–70 km depth. This conductor extends at least to the western edge of the profile where our magnetotelluric array ends, while its eastern edge lies beneath the trench outer rise wall. The anomalous layer is 1.5–2 times more conductive in the direction parallel to plate motion than parallel to the trench axis (Fig. 2b). The

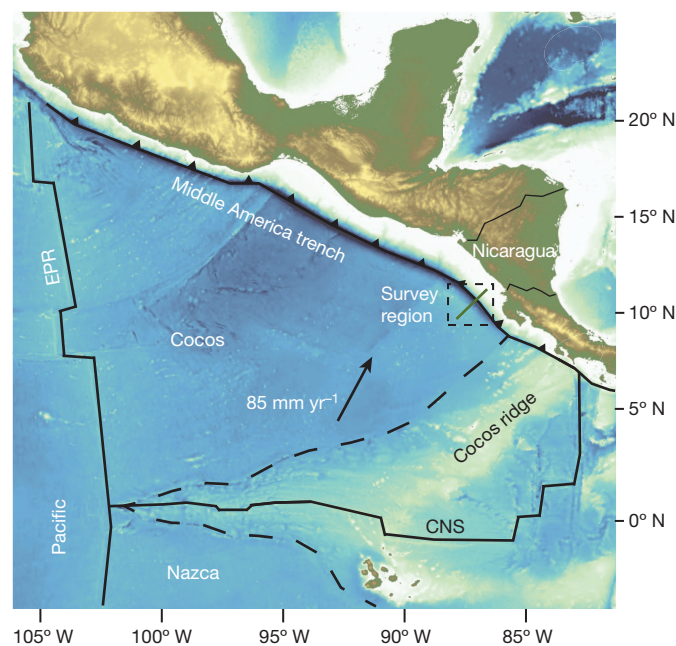


**Figure 1 | Regional tectonic map and location of the magnetotelluric survey.** The 280-km magnetotelluric profile (boxed) crosses the Middle America trench offshore of Nicaragua, where 23–24-Myr-old Cocos plate subducts beneath the Caribbean plate at a rate of 85 mm yr<sup>-1</sup>. The black dashed line separates the portions of the Cocos plate produced by either the East Pacific Rise (EPR) or the Cocos-Nazca spreading centre (CNS). The 50 sea-floor magnetotelluric stations were deployed at 10- and 4-km intervals in water depths ranging from 60 to 5,150 m and recorded magnetotelluric signals for 19 days during the month-long survey.

<sup>1</sup>Institute of Geophysics and Planetary Physics, Scripps Institution of Oceanography, University of California San Diego, La Jolla, California 92093, USA. <sup>2</sup>Department of Geology and Geophysics, Woods Hole Oceanographic Institution, Woods Hole, Massachusetts 02543, USA.

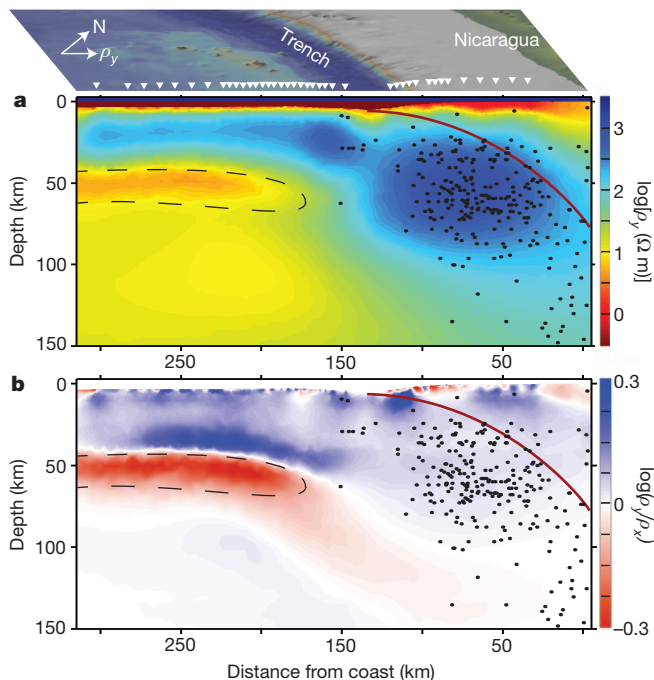


**Figure 2 | Resistivity model obtained from anisotropic inversion of the sea-floor magnetotelluric data.** At the top is the surface view; arrows show the direction of north and  $\rho_y$  (see below), and inverted triangles denote sea-floor magnetotelluric station locations. **a**, The electrical resistivity in the direction parallel to plate motion ( $\rho_y$ ). The colour scale gives  $\log[\rho_y (\Omega \text{ m})]$ , with blue and red colours corresponding to resistive and conductive (less resistive) features, respectively. The dark red line is a model of the top of the subducting slab<sup>30</sup>. Earthquake hypocentres from up to 50 km off-axis are shown as black circles (from the USGS/NEIC catalogue). The region enclosed by the dashed black line is where the model is at least 1.5 times more conductive in the direction parallel to plate motion. **b**, Resistivity ratio for the plate-motion-parallel ( $\rho_y$ ) to trench-axis-parallel ( $\rho_x$ ) model components. The colour scale gives  $\log(\rho_y/\rho_x)$ , and the plot shows the strong anisotropy of the conductive layer at 45–70 km depth (red regions >150 km offshore). Although the lithosphere above shows a strong anisotropy, we warn that this is not well constrained, because the magnetotelluric method is primarily sensitive to conductive rather than resistive features<sup>20</sup>. The deeper mantle beneath the conductive layer is isotropic, suggesting it is not being sheared.

deeper asthenosphere is isotropic, with resistivity 10–20  $\Omega \text{ m}$ . Model sensitivity studies indicate that the conductance (the product of conductivity and thickness) of the anisotropic conductive layer and the conductivity of the underlying isotropic asthenosphere are well constrained by the data (Supplementary Fig. 4). Because the magnetotelluric data are primarily sensitive to the layer conductance, the response of the observed anomalous layer, which is 25 km thick, is nearly equivalent to that from a 12.5 km layer with a conductivity twice as large; however, we favour the thicker layer found by the inversion because its higher resistivity requires less partial melt to explain it.

The anomalous layer is too conductive to be consistent with localized temperature variations, but could be explained by either a hydrated mantle or a small degree of partial melt. Mantle olivine with a water content of 800 parts per million (p.p.m.) has a similar conductivity to the observed layer<sup>11</sup> (Fig. 3a), but such a high water content would lead to significant partial melting over this depth range<sup>16</sup> (Fig. 3c). This leads us to conclude that the conductive layer must contain partial melt, arising from a mantle with a much lower degree of hydration.

Assuming a 23-Myr-old oceanic lithosphere with a mantle potential temperature of 1,420 °C, a partially molten peridotite matrix is stable beneath our profile (Fig. 3c)<sup>16,17</sup>. The top of the melting region at 45 km depth agrees with the intersection of the 23-Myr-old oceanic plate geotherm and a damp solidus containing  $275 \pm 85$  p.p.m.  $\text{H}_2\text{O}$ , signifying the minimum water content required for the stability of melt

to coincide with our observed high-conductivity layer. This intersection may culminate in a freezing front where melt solidifies owing to the colder temperatures above. We infer that this freezing front forms a permeability barrier that traps buoyant melt beneath, rather than allowing it to percolate to shallower depths. This barrier is further reinforced by the higher viscosity of the uppermost mantle above; this higher viscosity occurs because the uppermost mantle has been depleted of volatiles during upwelling and melting at the mid-ocean ridge<sup>18</sup>. This upper boundary may also represent a sharp increase in the solubility of water in mantle minerals, resulting in a corresponding sharp decrease in the stability of partial melt<sup>19</sup>.

Estimates derived from samples of mid-ocean ridge basalts give mantle  $\text{H}_2\text{O}$  contents of 50–200 p.p.m., which are too low for the 275 p.p.m.  $\text{H}_2\text{O}$  needed to sustain partial melts at 45 km depth. However, uncertainties in partition coefficient measurements may accommodate this discrepancy; the resulting statistical lower bound of 190 p.p.m.  $\text{H}_2\text{O}$  is within the range of estimates from mid-ocean-ridge basalts. We do not consider the effects that other volatiles (specifically,  $\text{CO}_2$ ) have on the solidus, which could further reduce the concentration of water required to induce silicate melts at 45–70-km depth<sup>8</sup>.

The electrical anisotropy indicates that the melt is made up of a network of tubes or elongated spheroids aligned in the direction of plate motion<sup>9</sup>. Hence, we estimate the amount of partial melt present by using a parallel mixing model appropriate for anisotropic conductivity, together with results of recent laboratory studies of hydrated basaltic melt conductivity<sup>10</sup>, yielding melt fractions of 1.0–2.1% for a mantle containing 275 p.p.m.  $\text{H}_2\text{O}$  (Fig. 3b). Further reductions in melt estimates are possible, but require water concentrations that may be unrealistically high. For instance, 0.3% melt is attained for a mantle with 720 p.p.m.  $\text{H}_2\text{O}$ . Likewise, carbonatite melt is significantly more conductive and thus yields even smaller fractions, but is an unlikely explanation because it is unstable at these depths<sup>8</sup>. Bulk conductivity in the deeper isotropic asthenosphere is best described by the Hashin–Shtrikman upper bound, which predicts well-connected melt fractions of 0.2–1.1% for the observed 10–20  $\Omega \text{ m}$  mantle.

Deep off-axis melt emplacement can occur during lithosphere formation at the ridge or result from accumulation of a small degree of intraplate melting<sup>8</sup>. An earlier magnetotelluric experiment at the southern East Pacific Rise spreading ridge observed an off-axis conductive asthenosphere at 60–120 km depth beneath a resistive lithosphere<sup>20,21</sup>. We interpret that conductive layer as requiring partial melt, because its conductivity and anisotropy are similar to observations beneath our profile (Fig. 3b). That portion of the ridge generates the Nazca plate; if we assume equivalent ridge processes are occurring for the Cocos plate, where our profile was measured, then most of the hydrous melt has been emplaced at or near the ridge axis. Additional melt may accumulate through deeper intraplate melting—for example, from small-scale convection<sup>22</sup>. Grain boundary migration of deeper partial melt<sup>23</sup> carries with it increased water content as a result of the preferential partitioning of water into silicate melts. As enriched hydrated melt rises, it collects beneath the colder, less permeable lithosphere<sup>24</sup> and shears into a network of interconnected horizontally aligned melt bands<sup>25</sup>, possibly driven by large-scale asthenospheric flow<sup>26</sup>. Stress gradients perpendicular to the shear direction have been shown to reduce the melt connectivity in the direction along the gradient<sup>9</sup>, offering a possible mechanism for our observed anisotropy. The depth extent over which the asthenosphere is being sheared can be inferred from the anisotropy of the melt layer along with its increased conductivity, which the magnetotelluric data constrain to a maximum thickness of 30 km.

The existence of a horizontally extensive melt layer that is being sheared over a confined depth interval indicates the LAB is a thin, low-viscosity channel. Theoretical studies suggest that even small melt fractions (<1%) can lower viscosity by up to two orders of magnitude, effectively decoupling the lithosphere from the asthenosphere<sup>27</sup>. The depth extent over which this decoupling occurs as well as its proximity

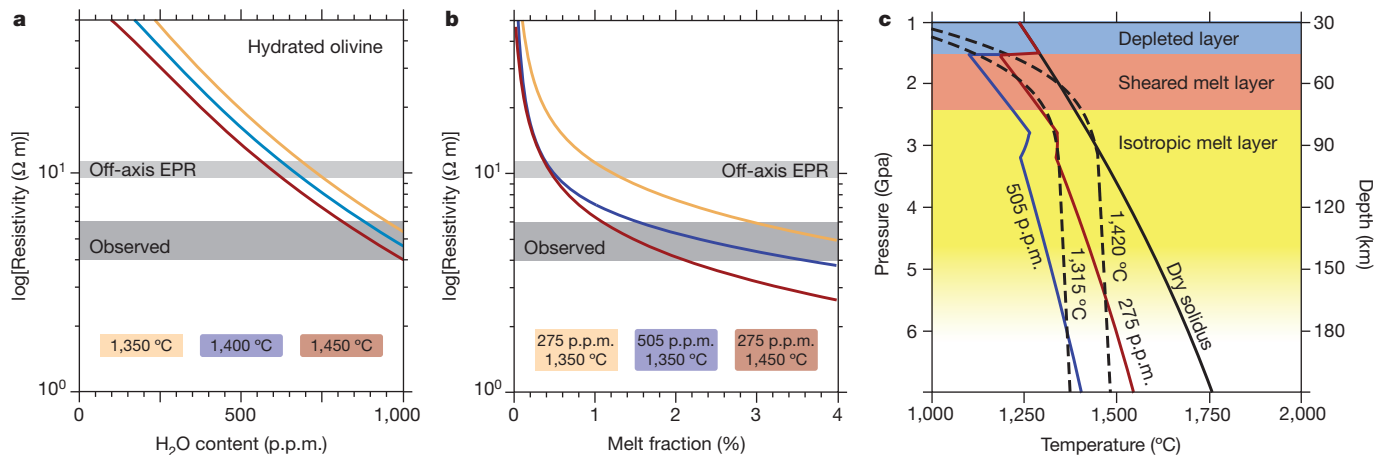


**Figure 3 | High asthenosphere conductivity explained by a thin partially molten layer.** Evidence for the stability of melt. **a**, Hydrated olivine resistivity is estimated as a function of H<sub>2</sub>O content for different temperatures<sup>11</sup>. The dark grey region represents the observed resistivity (4–6 Ω m) of the anomalous conductive layer, while the lighter grey region represents a 10 Ω m conductive layer observed off-axis at the southern EPR<sup>20</sup>. Olivine would be required to contain at least 800 p.p.m. H<sub>2</sub>O to account for the observed resistivity if no melt is present. **b**, Bulk resistivity of partial melt shown as a function of melt fraction for different temperatures and bulk mantle water contents<sup>10</sup> with an assumed

to the trench axis have potentially new implications for plate dynamics, as previous studies have focused on the effects of melt at the ridge axis and mantle wedge. A pervasive feature that exists beneath oceanic plates at large distances from spreading centres requires the stability of a partially molten layer, as dictated by the solidus of wet peridotite and a warm mantle geotherm. A previous magnetotelluric study of 140–150-Myr-old lithosphere in the Pacific Ocean basin did not find a conductive melt layer<sup>28</sup>. This is consistent with a thicker cold plate containing too little water to sustain hydrous melts at the greater LAB depth.

In our profile, the conductive layer ends near the trench, whereas the layer anisotropy persists in a trajectory that follows the subducting slab, albeit with a decreasing anisotropic factor. This signifies that as the plate subducts, some melt is likely to remain in place beneath the shallower LAB at the trench outer rise owing to its buoyancy. This offers an explanation in which the observed melt-rich LAB is caused by the concentration of low-fraction melts at the trench over time as the plate continues to be subducted; if this mechanism is responsible for locally enriching the asthenosphere with melt, we predict that melt would be most concentrated near the trench and decrease towards younger regions of the plate.

## METHODS SUMMARY

We processed the magnetotelluric data using a standard robust multi-station impedance estimation approach at periods of 22–32,000 s (ref. 29). Supplementary Fig. 1 presents the data and two-dimensional inversion model fits. The data subset suitable for two-dimensional modelling was evaluated by inspecting impedance polarization diagrams (Supplementary Fig. 2). Sites S31–S34, located on the margin slope near the base of the trench, display strong three-dimensional effects and were omitted entirely. The rest of the data exhibit a profile-wide rotation in strike angle at periods greater than 1,024 s that is incompatible with two-dimensional modelling and were also omitted.

The two-dimensional triaxially anisotropic inversion model was obtained using a standard inversion approach implemented using a new parallel adaptive finite element algorithm<sup>13,14</sup>. In addition to penalizing spatial variations in the model resistivity, the inversion included a penalty to minimize the amount of anisotropy produced in the inverted model. The data uncertainty was subject to a 10% error floor, with the inversion finding a smooth model with a root-mean-square (r.m.s.) misfit of 1.0 for the combined TE and TM mode data. Supplementary Fig. 3 shows the resistivity obtained for each coordinate axis.

Three tests were performed to investigate the sensitivity of the model to the interpreted features (Supplementary Fig. 4). All attempts significantly increased

mineral/melt partition coefficient of 0.006. **c**, Solid lines depict the solidus of dry and wet peridotite for various mantle H<sub>2</sub>O contents<sup>16</sup>. The dashed lines show the geotherms derived from a plate cooling model of 23-Myr-old oceanic lithosphere<sup>17</sup>. Melt is stable at depths greater than 45 km for peridotite with 275 ± 85 p.p.m. H<sub>2</sub>O and a 1,420 °C mantle potential temperature. A geotherm with a reduced mantle potential temperature of 1,315 °C requires 505 ± 155 p.p.m. H<sub>2</sub>O. The solidus of wet peridotite is calculated with the cryoscopic approximation assuming an oxide molar mass<sup>16</sup>.

the r.m.s. misfit, confirming the strong data sensitivity to the interpreted features of the converged model.

The solidus of wet peridotite was derived using the cryoscopic approximation with a molar enthalpy of fusion formulation (as described in ref. 16). The mole fraction of water in the melt was calculated with an oxide molar unit (59 g mol<sup>-1</sup>). The solidi are compared to geotherms calculated from a plate cooling model that has a 95-km-thick plate with a 1,420 °C or 1,315 °C mantle potential temperature for 23-Myr-old oceanic plate<sup>17</sup>.

Received 16 October 2012; accepted 28 January 2013.

- Rychert, C. A. & Shearer, P. M. A global view of the lithosphere-asthenosphere boundary. *Science* **324**, 495–498 (2009).
- Schmerr, N. The Gutenberg discontinuity: melt at the lithosphere-asthenosphere boundary. *Science* **335**, 1480–1483 (2012).
- Bagley, B. & Revenaugh, J. Upper mantle seismic shear discontinuities of the Pacific. *J. Geophys. Res.* **113**, B12301, <http://dx.doi.org/10.1029/2008JB005692> (2008).
- Nettles, M. & Dziewoński, A. M. Radially anisotropic shear velocity structure of the upper mantle globally and beneath North America. *J. Geophys. Res.* **113**, B02303, <http://dx.doi.org/10.1029/2006JB004819> (2008).
- Kawakatsu, H. *et al.* Seismic evidence for sharp lithosphere-asthenosphere boundaries of oceanic plates. *Science* **324**, 499–502 (2009).
- Anderson, D. L. & Sammis, C. Partial melting in the upper mantle. *Phys. Earth Planet. Inter.* **3**, 41–50 (1970).
- Karato, S. & Jung, H. Water, partial melting and the origin of the seismic low velocity and high attenuation zone in the upper mantle. *Earth Planet. Sci. Lett.* **157**, 193–207 (1998).
- Hirschmann, M. M. Partial melt in the oceanic low velocity zone. *Phys. Earth Planet. Inter.* **179**, 60–71 (2010).
- Caricchi, L., Gaillard, F., Mecklenburgh, J. & Le Trong, E. Experimental determination of electrical conductivity during deformation of melt-bearing olivine aggregates: implications for electrical anisotropy in the oceanic low velocity zone. *Earth Planet. Sci. Lett.* **302**, 81–94 (2011).
- Ni, H., Keppler, H. & Behrens, H. Electrical conductivity of hydrous basaltic melts: implications for partial melting in the upper mantle. *Contrib. Mineral. Petrol.* **162**, 637–650 (2011).
- Poe, B. T., Romano, C., Nestola, F. & Smyth, J. R. Electrical conductivity anisotropy of dry and hydrous olivine at 8 GPa. *Phys. Earth Planet. Inter.* **181**, 103–111 (2010).
- Key, K., Constable, S., Matsuno, T., Evans, R. L. & Myer, D. Electromagnetic detection of plate hydration due to bending faults at the Middle America Trench. *Earth Planet. Sci. Lett.* **351–352**, 45–53 (2012).
- deGroot-Hedlin, C. & Constable, S. Occam's inversion to generate smooth, two-dimensional models from magnetotelluric data. *Geophysics* **55**, 1613–1624 (1990).
- Key, K. & Ovali, J. A parallel goal-oriented adaptive finite element method for 2.5-D electromagnetic modelling. *Geophys. J. Int.* **186**, 137–154 (2011).
- Cox, C. S., Constable, S. C., Chave, A. D. & Webb, S. C. Controlled-source electromagnetic sounding of the oceanic lithosphere. *Nature* **320**, 52–54 (1986).

16. Hirschmann, M. M., Tenner, T., Aubaud, C. & Withers, A. C. Dehydration melting of nominally anhydrous mantle: the primacy of partitioning. *Phys. Earth Planet. Inter.* **176**, 54–68 (2009).
17. Stein, C. A. & Stein, S. A model for the global variation in oceanic depth and heat flow with lithospheric age. *Nature* **359**, 123–129 (1992).
18. Hirth, G. & Kohlstedt, D. L. Water in the oceanic upper mantle: implications for rheology, melt extraction and the evolution of the lithosphere. *Earth Planet. Sci. Lett.* **144**, 93–108 (1996).
19. Mierdel, K., Keppler, H., Smyth, J. R. & Langenhorst, F. Water solubility in aluminous orthopyroxene and the origin of Earth's asthenosphere. *Science* **315**, 364–368 (2007).
20. Evans, R. L. *et al.* Geophysical evidence from the MELT area for compositional controls on oceanic plates. *Nature* **437**, 249–252 (2005).
21. Baba, K., Chave, A. D., Evans, R. L., Hirth, G. & Mackie, R. L. Mantle dynamics beneath the East Pacific Rise at 17°S: insights from the Mantle Electromagnetic and Tomography (MELT) experiment. *J. Geophys. Res.* **111**, B02101, <http://dx.doi.org/10.1029/2004JB003598> (2006).
22. Ballmer, M. D., van Hunen, J., Ito, G., Tackley, P. J. & Bianco, T. A. Non-hotspot volcano chains originating from small-scale sublithospheric convection. *Geophys. Res. Lett.* **34**, L23310, <http://dx.doi.org/10.1029/2007GL031636> (2007).
23. Zhu, W., Gaetani, G. A., Fosseis, F., Montesi, L. G. J. & De Carlo, F. Microtomography of partially molten rocks: three-dimensional melt distribution in mantle peridotite. *Science* **332**, 88–91 (2011).
24. Katz, R. F. Magma dynamics with the enthalpy method: benchmark solutions and magmatic focusing at mid-ocean ridges. *J. Petrol.* **49**, 2099–2121 (2008).
25. Kohlstedt, D. L. & Holtzman, B. K. Shearing melt out of the Earth: an experimentalist's perspective on the influence of deformation on melt extraction. *Annu. Rev. Earth Planet. Sci.* **37**, 561–593 (2009).
26. Höink, T., Jellinek, A. M. & Lenardic, A. Viscous coupling at the lithosphere–asthenosphere boundary. *Geochem. Geophys. Geosyst.* **12**, Q0AK02 (2011).
27. Takei, Y. & Holtzman, B. K. Viscous constitutive relations of solid-liquid composites in terms of grain boundary contiguity: 1. Grain boundary diffusion control model. *J. Geophys. Res.* **114**, B06205, <http://dx.doi.org/10.1029/2008JB005850> (2009).
28. Matsuno, T. *et al.* Upper mantle electrical resistivity structure beneath the central Mariana subduction system. *Geochem. Geophys. Geosyst.* **11**, Q09003 (2010).
29. Egbert, G. D. Robust multiple-station magnetotelluric data processing. *Geophys. J. Int.* **130**, 475–496 (1997).
30. Hayes, G. P., Wald, D. J. & Johnson, R. L. Slab1.0: A three-dimensional model of global subduction zone geometries. *J. Geophys. Res.* **117**, B01302, <http://dx.doi.org/10.1029/2011JB008524> (2012).

**Supplementary Information** is available in the online version of the paper.

**Acknowledgements** We thank the captain (M. Stein) and crew of R/V *Melville* and the governments of Nicaragua and Costa Rica for permission to work in their exclusive economic zones. The following are thanked for their participation in the research cruise: C. Armerding, C. Berger, E. Carruthers, B. Cohen, J. Elsenbeck, T. Matsuno, D. Myer, A. Orange, J. Perez, K. Shadle, J. Souders, K. Weitemeyer, B. Wheelock and S. Zipper; J. Lemire and A. Jacobs are thanked for their efforts with cruise planning, mobilization and demobilization. We thank B. Wheelock and D. Hasterok for discussions. This work was supported by the National Science Foundation (grants OCE-08411141 and OCE-0840894) and the Seafloor Electromagnetic Methods Consortium at Scripps Institution of Oceanography.

**Author Contributions** K.K., R.L.E. and S.C. conceived the survey. K.K. and S.C. collected the data. S.N. and S.C. processed the data. S.N. analysed and inverted the data. S.N. and K.K. developed the interpretation and wrote the manuscript. All authors discussed the results and commented on the manuscript.

**Author Information** Reprints and permissions information is available at [www.nature.com/reprints](http://www.nature.com/reprints). The authors declare no competing financial interests. Readers are welcome to comment on the online version of the paper. Correspondence and requests for materials should be addressed to S.N. ([snaiif@ucsd.edu](mailto:snaiif@ucsd.edu)).